Journal of Hazardous Materials 354 (2018) 54–62

Contents lists available at ScienceDirect

Journal of Hazardous Materials

journal homepage: www.elsevier.com/locate/jhazmat

Biocompatible FeOOH-Carbon quantum dots nanocomposites for gaseous NO_x removal under visible light: Improved charge separation and High selectivity

Yu Huang[a,b,*], Yunxia Gao[a], Qian Zhang[a,b], Yufei Zhang[a,b], Jun-ji Cao[a,b], Wingkei Ho[c], Shun Cheng Lee[d]

[a] Key Laboratory of Aerosol Chemistry and Physics, Institute of Earth Environment, Chinese Academy of Sciences, Xi'an, 710061, China
[b] State Key Lab of Loess and Quaternary Geology (SKLLQG), Institute of Earth Environment, Chinese Academy of Sciences, Xi'an, 710061, China
[c] Department of Science and Environmental Studies, The Education University of Hong Kong, Hong Kong, China
[d] Department of Civil and Environmental Engineering, The Hong Kong Polytechnic University, Hong Kong, China

GRAPHICAL ABSTRACT

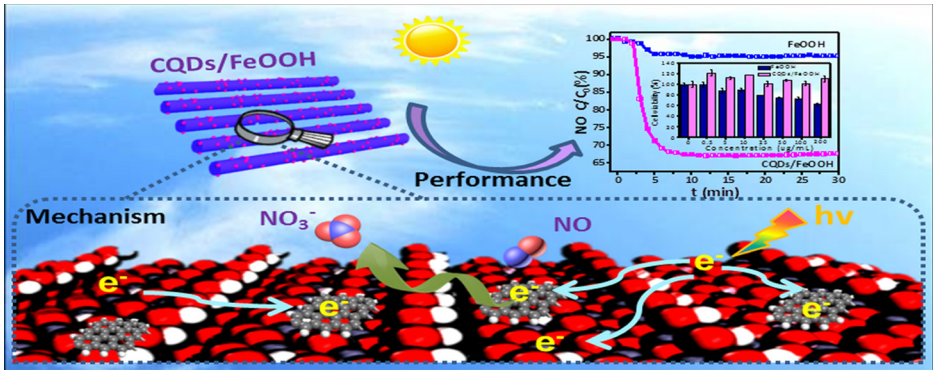

ARTICLE INFO

Keywords:
NOx purification
CQDs/FeOOH photocatalyst
DFT calculation
Charge carrier separation
Degradation mechanism

ABSTRACT

Development of biocompatible photocatalysts with improved charge separation and high selectivity is essential for effective removal of air pollutants. Iron-containing catalysts have attracted extensive attention due to their low-toxicity and high natural abundance. Here, carbon quantum dots (CQDs) modified FeOOH nanocomposites fabricated using a facile hydrothermal route showed enhanced NO removal efficiency (22%) compared to pure FeOOH. Moreover, generation of toxic NO_2 intermediates was significantly inhibited using the nanocomposites, demonstrating high selectivity for final nitrate formation. Photo-electrochemical results showed that both charge separation and transfer efficiency were significantly improved by CQDs addition, and the lifetime of photo-generated carriers was increased eventually. Density functional theory calculations further elucidated that the suppressed recombination of photo-induced electron-hole pairs was due to enhanced electron migration from the FeOOH to CQDs. A NO degradation mechanism was proposed based on detection of the reactive oxygen species using electron paramagnetic spectroscopy. In addition, the nanocomposite showed good biocompatibility and low cytotoxity, ensuring minimal environmental impact for potential application in large-scale.

* Corresponding author at: Key Laboratory of Aerosol Chemistry and Physics, Institute of Earth Environment, Chinese Academy of Sciences, Xi'an, 710061, China
E-mail address: huangyu@ieecas.cn (Y. Huang).

https://doi.org/10.1016/j.jhazmat.2018.04.071
Received 8 February 2018; Received in revised form 21 April 2018; Accepted 26 April 2018
Available online 27 April 2018
0304-3894/

1. Introduction

High concentrations of nitrogen oxides (NO_x) in the atmosphere contribute to environmental problems, such as acid rain and photochemical smog [1–3]. Hence, it is necessary to develop effective measures to control NO_x concentrations. Semiconductor photocatalysis offers an appealing route to remove NO_x at ambient concentration [4,5]. However, the development of economically feasible and eco-friendly photocatalysts with high efficiency remains a challenge.

Iron-containing catalysts have attracted extensive attention for NO_x removal as they have low toxicity, eco-friendliness, and high abundance in the Earth's crust [6–9]. Among the reported catalysts, iron (III) hydroxide (FeOOH) has been investigated for environmental pollution control due to its favorable band gap energy (~2.6 eV) allowing visible light activation [10]. Unfortunately, FeOOH usually suffers from severe charge recombination due to inherently poor electrical conductivity, which greatly hinders broad application [11,12]. Therefore, many studies have focused on optimizing charge migration in FeOOH by constructing heterostructures with FeOOH and other materials. Wang et al. fabricated interwoven Co_3O_4-carbon@FeOOH hollow polyhedrons; the optimized composition and structure showed significant enhancement of the electrochemical properties [13]. Recently, Li et al. designed FeOOH/CeO_2 and FeOOH/Co/FeOOH hetero-layered nanotube arrays for the oxygen evolution reaction; the unique hybrid structure resulted in low energy barriers of intermediates and low mass-transfer resistance, enhancing the catalytic reaction [14,15]. Moreover, electron acceptors are important for fast transfer of the photo-generated electrons, realizing effective light utilization and high quantum yields [16–18]. For example, H_2O_2 was ingeniously introduced as an electron acceptor into the precursor solution in the presence of FeOOH to improve the photocatalytic activity [19]; H_2O_2 efficiently trapped electrons and increased the generation of hydroxyl radicals. Various high-conductivity materials, such as Au, CNT, and rGO, can be coupled with FeOOH to enhance the photocatalytic activity for pollutant degradation [20–23].

The conjugated π structures of carbon quantum dots (CQDs) make them excellent electron transporters and acceptors [24], while the up-converted photoluminescence (UCPL) effect allows them to absorb solar radiation over a wide range of wavelengths (ultraviolet to infrared). In CQDs/TiO_2 composite photocatalysts, the CQDs convert visible or infrared light to shorter wavelengths via the UCPL effect and enhance electron transfer along specific directions [25,26]. Recently, various CQDs-containing nanocomposites were fabricated and showed improved photocatalytic activity, such as CQDs/metal oxide (CQDs/Fe_2O_3, CQDs/ZnO, and CQDs/SiO_2) [27–30], CQDs/metal (CQDs/Au, CQDs/Cu) and ternary CQDs/metal/semiconductor (CQDs/Ag/Ag_3PO_4 and CQDs/Ag/$Ag_3PW_{12}O_{40}$) [31–33] composites. The CQDs in the nanocomposites promote the transfer of photoelectrons and hinder the recombination of charge carriers [34–36]. However, few studies discussed the effect of electron transfer direction and the relative contributions of UCPL and charge separation, which are critical for explaining the high photocatalytic activity.

Herein, we developed cost-effective spicule CQDs/FeOOH nanocomposite photocatalysts using a facile hydrothermal process and tested them for NO_X removal at ambient levels. Through comprehensive experimental characterization and density functional theory (DFT) calculations, we compared the photocatalytic behavior of the CQDs/FeOOH composites with that of pure FeOOH and discuss potential mechanisms.

2. Experimental

2.1. Synthesis of CQDs/FeOOH nanocomposites

All reagents were of analytical grade and used without further purification. The CQDs/FeOOH nanocomposites were synthesized using a hydrothermal route by adding various amounts of CQDs to an iron precursor solution. Specifically, 12 mmol of Fe $(NO_3)_3{\cdot}9H_2O$ was dissolved in 20 mL of deionized water; then, 48 mmol of KOH solution was added dropwise under vigorous stirring. The dispersed suspension was sonicated for 30 min and different volumes of a CQDs solution were added. Subsequently, a mixture with 2.5 vol % CQDs was placed in a 50 mL Teflon-lined stainless steel autoclave and kept at 100 °C for 6 h. The as-prepared nanocomposites were purified by washing with distilled water and absolute ethanol, and then dried in a vacuum oven at 70 °C for 24 h. The CQDs/FeOOH nanocomposites with 1.5%, 2.0%, 2.5% and 3.0% (vol %) CQDs were fabricated and designated as C-Fe-1.5, C-Fe-2.0, C-Fe-2.5, and C-Fe-3.0, respectively. For comparison, pure FeOOH was prepared under the same conditions. The CQDs used here were synthesized as reported previously [37] (see Supplementary Information for details).

2.2. Materials characterization

The crystal structures of the samples were characterized by X-ray diffraction (XRD; PANalytical X'pert, Netherlands) using Cu Kα radiation (λ = 1.5406 Å). The surface chemical states of the samples were analyzed using X-ray photoelectron spectroscopy (XPS; Thermo Escalab 250Xi, USA) with monochromatic Al Kα X-rays ($h\nu$ = 1486.71 eV). Field-emission scanning electron microscopy (FE-SEM; JSM-6700F, Japan) and high-resolution transmission electron microscopy (HR-TEM; JEOL JEM-3010, Japan) were employed to investigate the morphology. N_2 adsorption–desorption isotherms were obtained at 77 K using a Gemini VII 2390 analyzer (Micromeritics Instrument Corp., USA) and used to calculate the Brunauer-Emmett-Teller (BET) surface areas. The optical properties were obtained using a Varian Cary 100 Scan UV–vis system (UV–vis; Agilent Corp., USA) using Ba_2SO_4 reflection as a reference. Photoluminescence (PL) and steady and time-resolved fluorescence emission spectra were recorded using a fluorescence spectrophotometer (FLS-980, Edinburgh Instrument Ltd., UK). Electron spin-resonance spectroscopy (ESR; JEOL, JES-FA200, Japan) was undertaken on samples prepared by mixing the as-prepared photocatalyst in a 25 mM DMPO (5,5′-dimethyl-1-pirroline-*N*-oxide) solution with 50 mL of an aqueous dispersion for DMPO-·OH and 50 mL of a methanol dispersion for DMPO-·O_2^-.

2.3. Photocatalytic NO removal

The photocatalytic activity of the as-prepared samples was investigated by removing NO at ppb levels in a continuous flow reactor composed of a 4.5 L rectangular stainless steel vessel with a quartz glass top panel. Simulated solar light was supplied by a 300 W xenon lamp and a UV cutoff filter ($\lambda > 420$ nm) was used to obtain visible light. The light intensity on the sample surface was measured to be 28.29 mW/cm^2 (Thorlabs PM100D, USA), and the photocatalytic performances of all samples were estimated under identical test conditions. The lamp was positioned vertically above the quartz window. For each experiment, 0.1 g of photocatalyst powder was dispersed in 30 mL of distilled water and placed in a 12.0 cm diameter dish, which was preheated at 60 °C to remove water, cooled to room temperature, and then placed at the center of the reactor. The NO gas was supplied from a compressed gas cylinder at a concentration of 50 ppm and diluted to 400 ppb during testing with air from a zero air generator (Model 1001, Sabio Instruments LLC, USA). Here, the gas stream with a flow rate of 3 L/min was introduced to the chamber in the dark, and the residence time of NO is 36 s. When adsorption–desorption equilibrium was achieved, the xenon lamp was turned on and the NO and NO_2 concentrations were continuously monitored. The removal ratio of NO is expressed as C/C_0 (%), where C is the NO concentration (ppb) at any given time and C_0 is the initial NO concentration (ppb).

2.4. DFT calculations

All first-principles DFT calculations were implemented using the Cambridge Sequential Total Energy Package (CASTEP) code with the plane-wave Vanderbilt-type ultra-soft pseudopotentials approach [38]. The generalized gradient approximation (GGA) with Perdew-Burke-Ernzerh (PBE) function was used to account for the exchange-correlation potentials and electron-electron interactions [39]. The kinetic cut-off energy was 400 eV for all calculations and the self-consistent field convergence criterion was 1.0×10^{-5} eV. For optimization of the geometry, the convergence criteria of the energy change and residual force were less than 1.0×10^{-5} eV/atom and 0.1 eV/A, respectively. For bulk FeOOH, the Brillouin zone was sampled in a $2 \times 2 \times 2$ Monkhorst-pack k point grid geometry optimization. In addition, a $1 \times 1 \times 2$ Brillouin zone mesh was employed to obtain the geometry and density of states (DOS) of CQDs/FeOOH. The charge-transfer properties were calculated from the electron density difference (EDD) based on Miliken population analysis.

2.5. Cytotoxicity assay

The cytotoxicity was evaluated by testing human alveolar epithelial (A549) cell growth using a standard methyl thiazolyltetrazolium (MTT) assay. The optical density (OD) was recorded at 490 nm using a microplate reader (Multiskan GO, Thermo Scientific Inc., USA), and each measurement was performed in triplicate. The cell viability was $OD_{treated}/OD_{control}$ (%), where $OD_{treated}$ and $OD_{control}$ are the obtained optical density with and without photocatalyst, respectively. More details appear in the Supplementary Information.

3. Results and discussion

3.1. Phase structure and surface elemental composition

The powder XRD patterns of the as-prepared C-Fe-2.5 nanocomposite and the pristine α-FeOOH samples are shown in Fig. 1a. Typical diffraction peaks were located at 2θ values of 21.2°, 33.2°, 36.6°, 41.3°, and 53.3° corresponding to the (110), (130), (111), (140), and (221) planes of orthorhombic goethite α-FeOOH with a unit cell of a = 4.608, b = 9.956, and c = 3.022 Å (JCPDS file No. 29–0713). No other impurity peaks were detected, suggesting that pure α-FeOOH was synthesized. The C-Fe-2.5 composite showed α-FeOOH peaks with lower intensity than pure FeOOH, while we observed no diffraction peaks for the CQDs (2θ–26.0°) [40], probably due to the low concentration and crystallinity of the CQDs in the composite (consistent with other studies) [41,42]. The position of the FeOOH peak was very similar for the composite, implying that the presence of CQDs had no significant effects on goethite lattice [43].

XPS analysis was performed to verify the existence of CQDs on the FeOOH and characterize the chemical composition of C-Fe-2.5. The survey spectrum of C-Fe-2.5 (Fig. 1b) shows Fe, O, and C as main components. Fig. 1c shows the high-resolution C 1*s* spectrum of C-Fe-2.5, which was deconvoluted into three major peaks. Typically, the peak at 284.6 eV is attributed to the C—C bond of the sp^2 orbital, and the peaks at 286.0 and 287.8 eV are assigned to the sp^3 hybridized carbons from —COOH moieties, which may be derived from the surface functional groups on the CQDs. In the Fe 2*p* region (Fig. 1d), the binding energies located at 724.0 and 710.2 eV corresponded to the Fe $2p_{1/2}$ and Fe $2p_{3/2}$ orbitals of Fe^{3+}, respectively. For the nanocomposite, the corresponding peaks located at 724.3 and 710.4 eV, which is positive shift 0.3 and 0.2 eV for Fe $2p_{1/2}$ and Fe $2p_{3/2}$ orbitals. In addition, the O 1*s* spectrum of pure FeOOH and C-Fe-2.5 are shown in Fig. 1e. The two peaks centered at 528.9 and 530.2 eV are associated with Fe—O—Fe and Fe—O—H bonds in FeOOH, respectively, and that at 532.1 eV is the characteristic signal of oxygen in surface hydroxyl groups [12,44,45]. Compared with the pure FeOOH, those peaks for Fe—O—Fe and Fe—O—H shift by ~0.4 eV and ~0.3 eV toward higher binding energy. The increased in binding energy of XPS peaks can be caused by the decreased electron density. Meanwhile, these peaks shift further evidence the successful introduction of CQDs on the surface of α-FeOOH, and suggested the strong electron interactions between FeOOH and CQDs [20]. The UV–vis absorption spectra of the as-prepared samples are shown in Fig. 1f; it is clear that the pristine FeOOH harvested most of the UV and visible light. By extrapolating the linear part of the $(ahv)^2$ vs. photon energy curve (where a is the absorption coefficient), the bandgap energy was estimated to be 2.1 eV (see Fig. S1) [46]. After CQDs modification, the absorption strength increased, particularly in the visible region, suggesting CQDs are an outstanding optical response material.

3.2. Morphology

The morphology of the pure FeOOH, pure CQDs, and C-Fe-2.5 composite were investigated using SEM (see Supplementary Information) and TEM. As shown in Fig. S2a and b, the as-prepared FeOOH showed a homogeneous spicule structure ~600 nm in length and ~50 nm in width. This morphology was confirmed by the TEM results (Fig. 2a). The spicules had a lattice spacing of 0.25 nm, consistent with the *d*-spacing of the (111) plane of FeOOH (Fig. 2b). The as-prepared CQDs nanoparticles showed the typical spherical structure with a diameter of 5–10 nm (Fig. 2c). HR-TEM images (inset, Fig. 2c) showed a lattice spacing of 0.34 nm, attributed to the (002) plane of graphite carbon, verifying that graphite-phase CQDs were obtained. The spicule structure of FeOOH was preserved after CQDs addition, while this nano-structure tended to aggregate (see Fig. S2c and d). Note, that the specific BET surface area of FeOOH increased dramatically after CQDs modification, reaching 130.6 m^2/g, four times higher than that of pristine FeOOH (32.0 m^2/g); see Table S1. We propose that the agglomeration was responsible for changes in the surface properties. Fig. 2d and e show TEM images of C-Fe-2.5, where the CQDs were scattered on the FeOOH surface (Fig. 2d). The HR-TEM analysis (Fig. 2e) confirmed the presence of FeOOH in accordance with the corresponding fast Fourier transformation (FFT) shown in Fig. 2f. Overall, the XPS and HRTEM results indicated successful preparation of CQDs/FeOOH nanocomposites; it is expected that the intimate surface contact between the FeOOH and CQDs would be advantageous for efficient interfacial charge migration.

3.3. Photocatalytic activity for NO degradation

The photocatalytic NO removal efficiency of as-prepared CQDs/FeOOH nanocomposites was tested under simulated solar and visible light irradiation (λ > 420 nm). Fig. 3 shows C/C_0 (%) values vs. irradiation time (t) for the various photocatalysts. Obviously, no nitric oxide can be converted in the absence of photocatalyst under visible light irradiation. Here, the photo-degradation efficiency of the commercial P25 was also evaluated. For pure FeOOH, it showed negligible NO removal efficiency under visible light irradiation compared with P25, attributed to a high recombination rate. In comparison, the NO removal efficiency increased substantially after introducing CQDs, suggesting that the as-prepared CQDs/FeOOH nanocomposites have a good development potential for air purification. when the CQDs loading increased from 1.5 to 2.5%, the NO degradation efficiency was enhanced. The optimal NO removal ratio was obtained at 2.5 vol % CQDs loading, where nearly 22% of initial NO was removed within 30 min. However, a further increase to 3 vol % CQDs loading resulted in an obvious decrease in NO removal. The CQDs/FeOOH composites showed a similar trend in NO removal under simulated solar light (Fig. S3), with C-Fe-2.5 showing the best performance (~34% of the initial NO was removed). The enhanced photocatalytic activity is attributed to the excellent electron conductivity of the CQDs and suppression of recombination of photoinduced carriers from FeOOH.

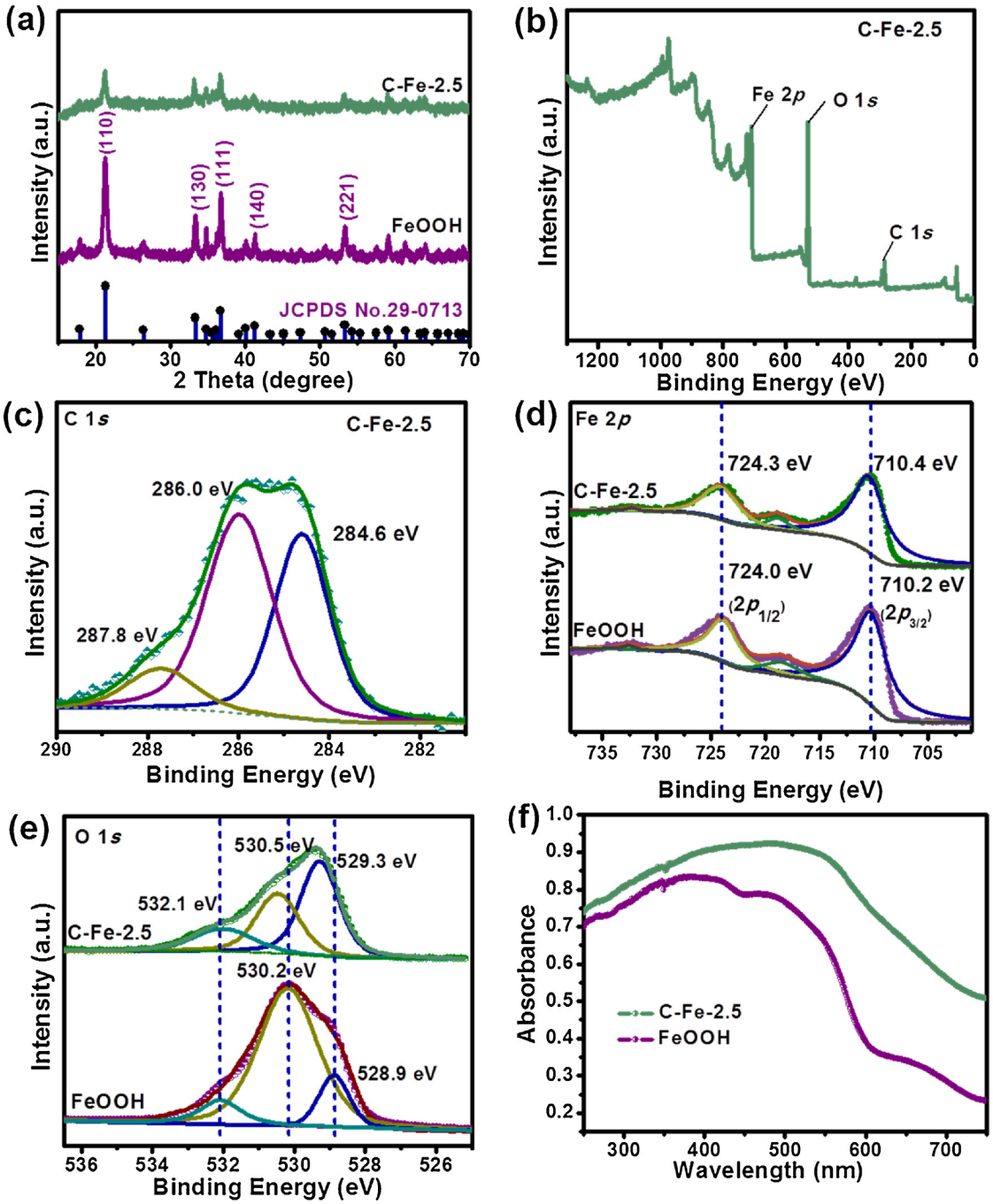

Fig. 1. (a) XRD patterns of pristine FeOOH and C-Fe-2.5. (b) XPS survey spectrum of C-Fe-2.5. (c) C1*s* spectrum of C-Fe-2.5. (d) Fe2*p* spectrum of FeOOH and C-Fe-2.5. (e) O1*s* spectrum of FeOOH and C-Fe-2.5. (f) UV–vis absorbance curve of FeOOH and C-Fe-2.5.

It has been reported that NO_2 (a byproduct of photocatalytic degradation of NO) is much more toxic than NO [47,48]. Therefore, NO_2 yields during NO degradation were monitored simultaneously (Fig. S4a and b). The concentration of NO_2 intermediates was below 6 ppb for all composite photocatalysts in comparison with commercial P25, suggesting that the initial NO (at 400 ppb) was largely transformed into NO_3^- for CQDs/FeOOH nanocomposites instead of NO_2. Fig. S5a shows the results of multiple photocatalytic NO removal runs using C1−Fe-2.5 to demonstrate the photocatalytic stability. A small reduction in activity between the first and fifth runs was observed, indicating that the material was relatively unstable for long-term use. The used photocatalyst was refreshed by washing in deionized water; retesting showed that the activity was recovered (sixth run). Moreover, the XRD spectra of the used composite were unchanged, illustrating that the catalyst was structurally stable (see Fig. S5b). The reduced activity probably arose from the accumulation of NO_3^- on the catalyst surface, impeding the NO reaction.

3.4. Charge separation and charge transfer mechanism

The main reason for the poor photocatalytic performance of pure FeOOH was rapid recombination of the photo-induced carriers; hence, the charge separation was evaluated using transient photocurrent density vs. time curves (Fig. 4a). When the light source was turned on, the current density of C-Fe-2.5 rapidly increased to 1.12 μA/cm^2 and remained stable until the light was switched off. The photocurrent

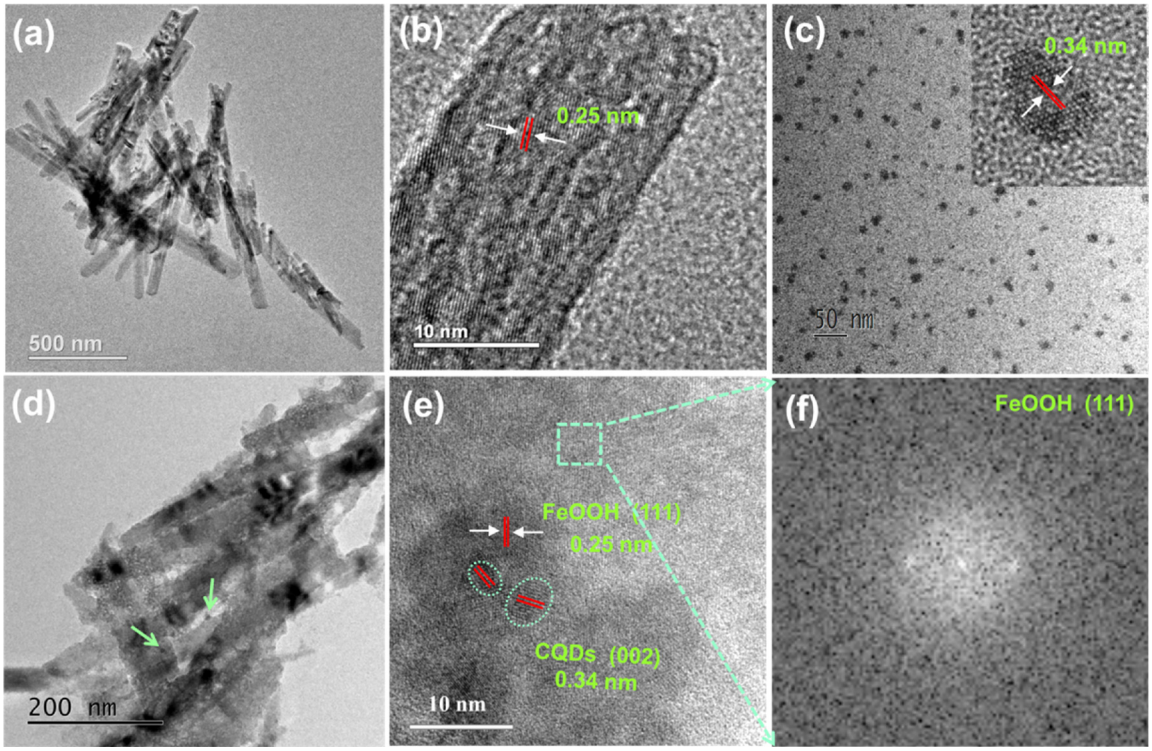

Fig. 2. (a) TEM and (b) HR-TEM images of pure FeOOH. (c) TEM and HR-TEM (inset) images of CQDs nanoparticles. (d) TEM and (e) HR-TEM images of C-Fe-2.5. (f) FFT corresponding to the region inside the green box in (e) (For interpretation of the references to colour in this figure legend, the reader is referred to the web version of this article).

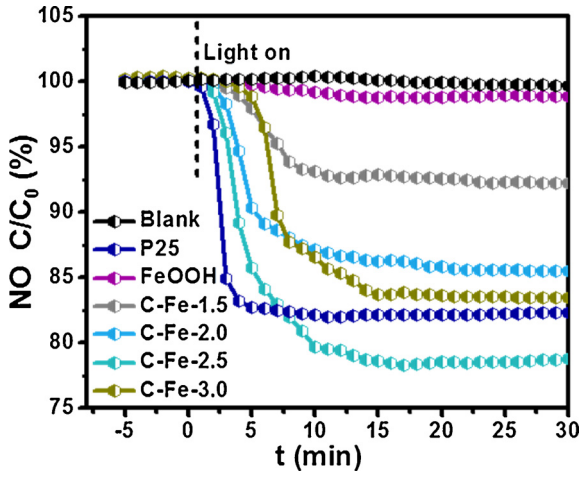

Fig. 3. Photocatalytic NO degradation efficiency (C/C_0, %) vs. irradiation time (t) under visible light ($\lambda > 420$ nm) over pure FeOOH, CQDs/FeOOH nanocomposites with different CQDs loadings, and P25.

density was 3.3 times higher than that of pure FeOOH (0.34 μA/cm^2), suggesting that the CQDs promoted charge separation. This was confirmed by photoluminescence (PL) spectra where C-Fe-2.5 exhibited a weaker PL signal than pure FeOOH, indicating efficient reduction of charge recombination (see Fig. S6). Moreover, EIS data of the as-prepared samples (Fig. 4b) showed that the semicircle in the Nyquist plot for C-Fe-2.5 was much smaller than that of pure FeOOH, indicating a lower charge transfer resistance. Hence, the CQDs are thought to enhance separation and transfer of photo-induced carriers.

To compare the photo-excited carrier kinetics of FeOOH before and after CQDs modification, nanosecond-level time-resolved fluorescence spectroscopy was performed (Fig. 4c). The fluorescence decay spectra were collected at 562 nm, and the fitted results are listed in Table S2; the radiative lifetime of pure FeOOH was 0.38 ns, slightly shorter than that of the composites (0.43 ns). Therefore, we propose that the prolonged lifetime of photoinduced carriers resulted from enhanced charge separation and a higher probability of the carriers participating in the photocatalytic reaction.

In general, CQDs can absorb the visible and infrared light and emit the shorter wavelength light through the unique UCPL effect. In this paper, Fig. 1f showed that the bare FeOOH has a strong absorption in ultraviolet and visible region, and thus we considered that the UCPL effect derived from infrared region should be a significant behavior after all the strong visible light response of FeOOH obscuring the emitted light from UCPL fluorescence. Here, to compare the difference between solar light and absence infrared light or to verify whether the UCPL effect played a role in our system, we conducted a control experiment under irradiation at a cut-off wavelength of 800 nm. Fig. S7 show that the NO removal rate for C-Fe-2.5 was ~30% at $\lambda < 800$ nm, which was 3% lower than when exposed to the full solar spectrum (33%). Therefore, UCPL due to infrared light played a secondary role (~9.1%) in NO photodegradation.

To further elucidate the charge carrier transfer between FeOOH and CQDs, DFT calculations were performed by calculating the electron density difference (EDD) of CQDs/FeOOH composites. Crystal models of the FeOOH and CQDs are shown in Fig. 5a and b, respectively, where the hybrid structure was composed of the FeOOH (111) plane with a sheet of CQDs (Fig. 5c). After geometrical optimization, a slight incline in the CQDs sheets towards the FeOOH appeared (Fig. 5d). This change resulted in charge redistribution at the interface (see the EDD plot in Fig. 5e). There were 0.38 electrons transferred from the FeOOH to CQDs at the interface. To gain an insight into the driving force of electron transfer from FeOOH to CQDs, the energy band structure, total density of states (TDOS) and partial density of states (PDOS) of FeOOH and CQDs over the nanocomposites were investigated in Fig. S8. Obviously, partial energy levels of CBM over the DOS of FeOOH are higher than that of CQDs, which supply the driving force of electron transfer

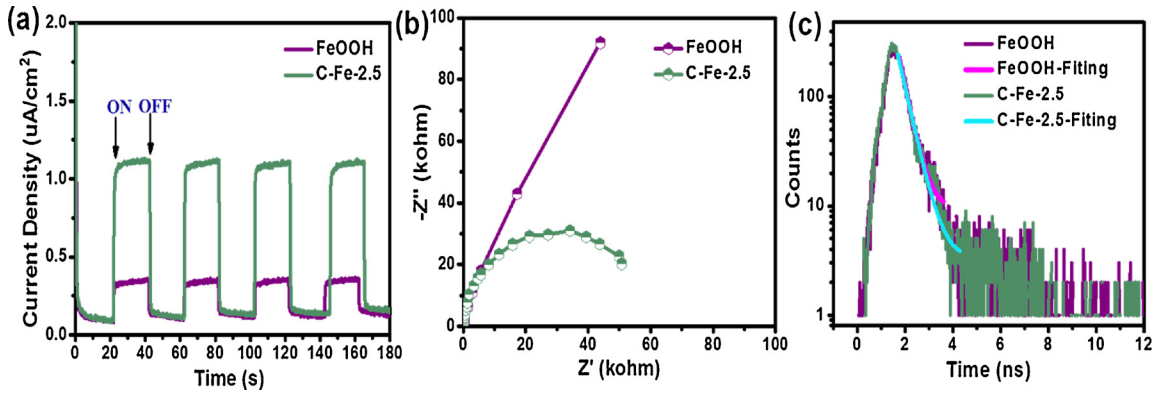

Fig. 4. (a) Transient photocurrent density vs. time curves of pure FeOOH and C-Fe-2.5 electrodes at 0.2 V vs. Ag/AgCl in Na_2SO_3 (0.1 mol/L) under simulated solar light irradiation. (b) EIS spectra of sample electrodes measured in a 1 mmol/L $K_3Fe(CN)_6$-$K_4Fe(CN)_6$ solution with applied voltage of 5 mV. (c) nanosecond-level time-resolved transient PL decay curves for pure FeOOH and C-Fe-2.5.

from FeOOH to CQDs. In addition, Fe3*d* and C2*p* states mainly contribute to the TDOS of FeOOH and CQDs, respectively. Thus, electron transitions occur mainly in Fe3*d* and C2*p* orbitals. The above results are consistent with the EDD results of CQDs/FeOOH. These theoretical results were consistent with the experimental findings, confirming that the CQDs primarily served as the main electron transfer path and facilitated charge separation [49].

3.5. Active species and oxidation mechanism

The role of reactive oxygen species during photocatalytic NO removal was detected through DMPO spin-trapping ESR spectroscopy (Fig. 6a and b). No signal was detected when the photocatalyst suspension was in the dark, i.e., no active radicals were generated on either FeOOH or C-Fe-2.5. Under simulated solar light illumination for 8 min, the signals of DMPO-$\cdot O_2^-$ with sextet peaks and DMPO-OH with quartet peaks were observed for C-Fe-2.5, which were remarkably enhanced compared to those of pure FeOOH. Hence, both O_2^- and ·OH radicals participated in NO removal.

Mott-Schottky plots used to derive the band-edge positions of FeOOH demonstrated the generation of radicals (Fig. S9). The flat-band potential (V_{fb}) of FeOOH was −0.35 V vs. NHE at pH 7 [50]. Using the bandgap measured from UV–vis spectroscopy, the position of the CB and VB for FeOOH was -0.35 V and 1.75 V vs. NHE, respectively. The photoelectrons in the CB of FeOOH reduced O_2 to $\cdot O_2^-$ as $E^\circ(O_2/\cdot O_2^-)$ was about −0.33 eV (Eq. (3)), whereas VB holes were not positive

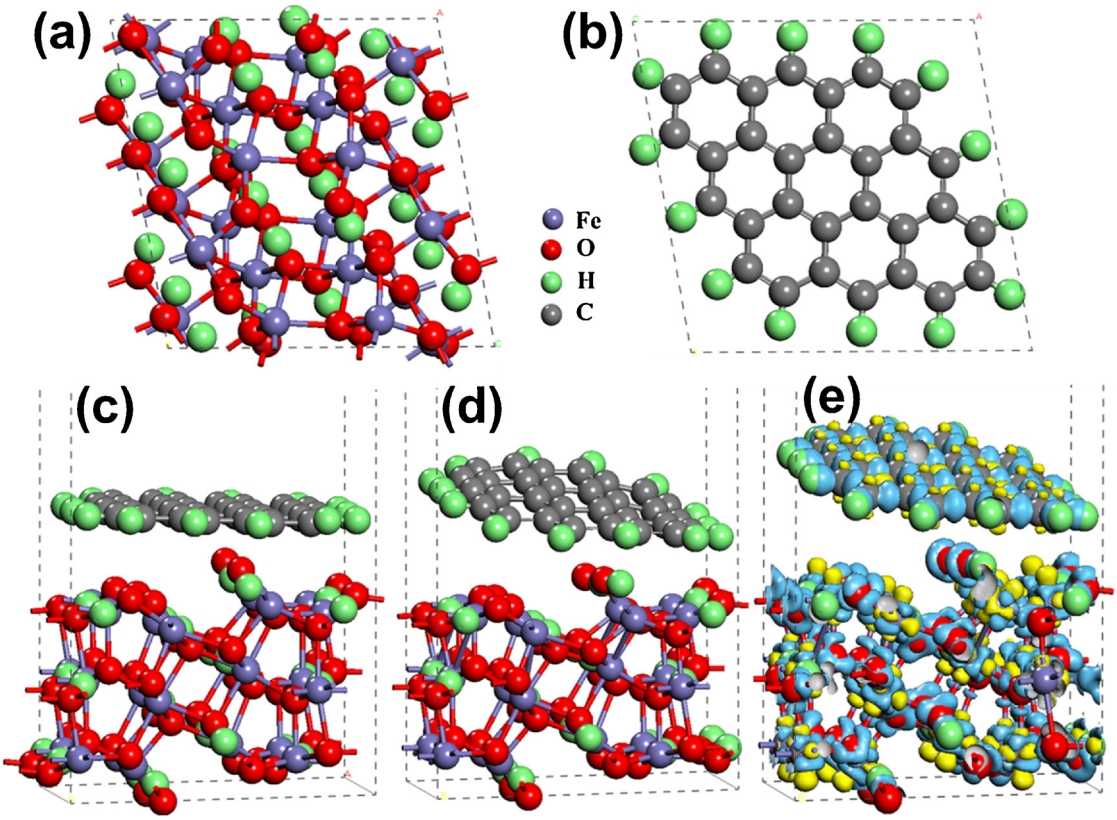

Fig. 5. Crystal models of (a) FeOOH, (b) CQDs, and (c) CQDs/FeOOH nanocomposite used in the DFT calculations. (d) The optimized crystal structure and (e) calculated electron density difference of the CQDs/FeOOH composite where the blue and yellow regions show electron density accumulation and depletion, respectively (For interpretation of the references to colour in this figure legend, the reader is referred to the web version of this article).

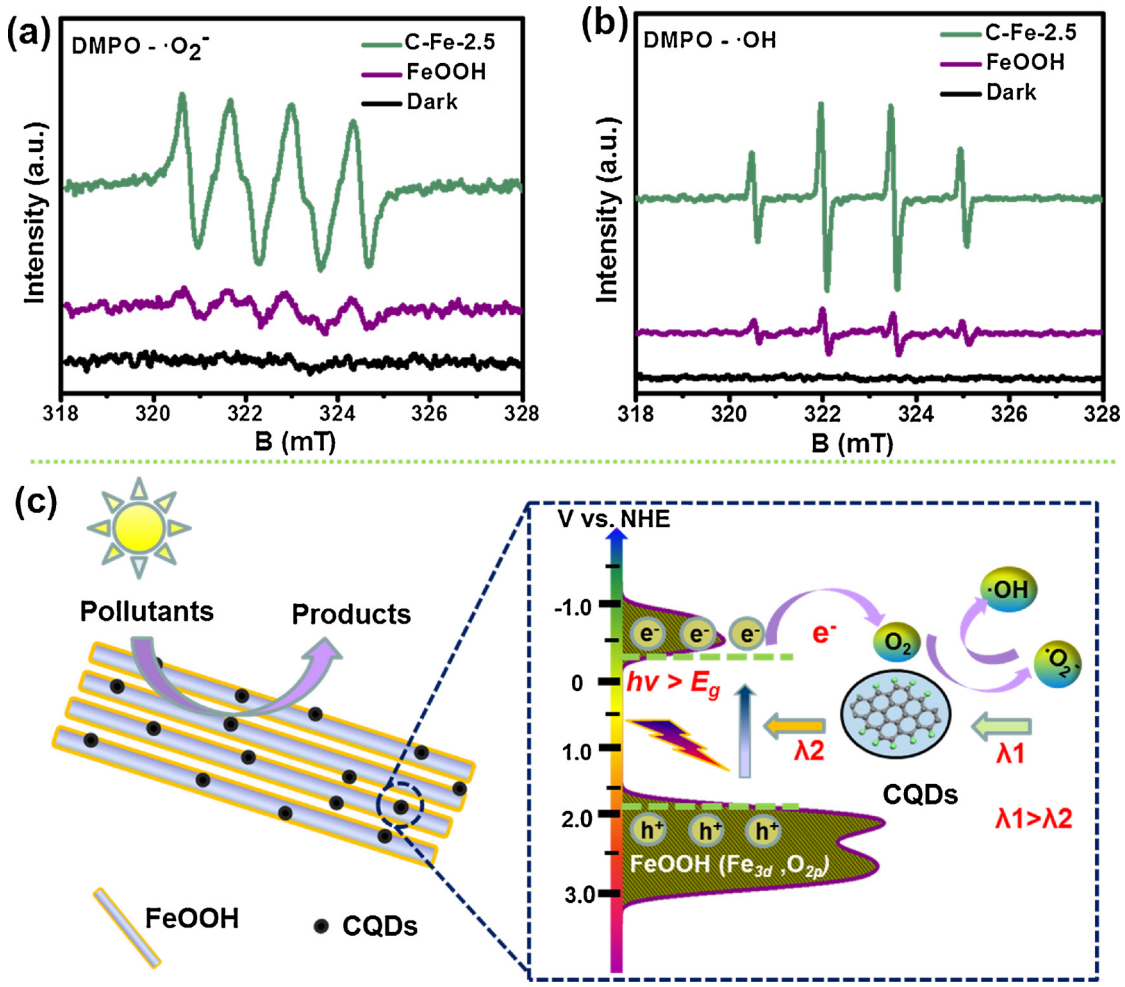

Fig. 6. DMPO spin-trapping ESR spectra of FeOOH and C-Fe-2.5 with or without 8 min illumination of simulated solar light: (a) DMPO-·O_2^- and (b) DMPO-·OH peaks; (c) Schematic diagrams of photo-induced electron separation and transfer over CQDs/FeOOH photocatalyst.

enough to generate ·OH radicals as E°(·OH/OH^-) was + 1.99 eV vs. NHE. Hence, the observed ·OH signal was most likely from the reduction of ·O_2^- via the ·O_2^-→H_2O_2→·OH route (Eq. (4) and (5)). Modification with CQDs prolonged the photoelectron lifetime, thereby increasing the concentration of radicals.

In general, the photocatalytic performance is positive correlation with specific surface area. However, in this work, the increased specific surface area of FeOOH showed non-significant contribution to the activity enhancement. As observed (Table S1 and Fig. 3), the surface area for C-Fe-2.5 is 130.6 m^2/g and that of for C-Fe-2.0 is 127.2 m^2/g. However, the NO removal efficiency of C-Fe-2.5 (22%) is apparently higher than that of C-Fe-2.0 (15%). Furthermore, when the loading amount of CQDs increased to 3 vol %, C-Fe-3.0 obtained the maximum BET surface area (151.0 m^2/g), but it showed decreased NO degradation efficiency than that of C-Fe-2.5. Therefore, in this work, the appropriate loading amount of CQDs is the major contributor for NO activity enhancement rather than the specific surface area enlargement. On account of the inherent defects of FeOOH which often suffers from the severe charge recombination and the poor electron transfer capability, we propose that the improved optical absorption and charge separation of the composite are responsible for the high NO removal efficiency [51]. Considering the experiment and theoretical results, we propose the following NO oxidation pathways and the photocatalytic NO degradation mechanism shown in Fig. 6c.

$$FeOOH + hv \rightarrow FeOOH^* \quad (1)$$

$$FeOOH^* + CQDs \rightarrow FeOOH\ (h^+) + CQDs\ (e^-) \quad (2)$$

$$CQDs\ (e^-) + O_2 \rightarrow \cdot O_2^- \quad (3)$$

$$\cdot O_2^- + 2H^+ + e^- \rightarrow H_2O_2 \quad (4)$$

$$H_2O_2 + e^- \rightarrow \cdot OH + OH^- \quad (5)$$

$$\cdot O_2^-/\cdot OH + NO \rightarrow NO_2/NO_3^- + H_2O/H^+ \quad (6)$$

Under solar irradiation, electrons are excited from the VB to the CB of FeOOH, generating electron-hole pairs (Eq. (1)). CQDs are excellent electron conductors and collect electrons from FeOOH and immediately generate active species, ·O_2^- and ·OH (Eqs.(2)–(5)). Besides, the partial emitted light from the UCPL effect of CQDs also play a synergistic role in photoelectron excitation. Subsequently, the absorbed NO is oxidized to NO_3^- by these active species (Eq. (6)) [52].

3.6. Cell cytotoxicity assay

Considering the practical applications of CQDs/FeOOH nanocomposites, an authentic MTT assay with A549 cells was performed to assess the biocompatibility of the composite. Fig. 7 shows that the cell viability decreased by 63% with increasing FeOOH concentration from 0.5 to 200 μg/mL. However, the cell viability of C-Fe-2.5 increased with increasing composite concentration and exceeded that of the pure control solution, indicating good biocompatibility and low cytotoxicity for A549 cells.

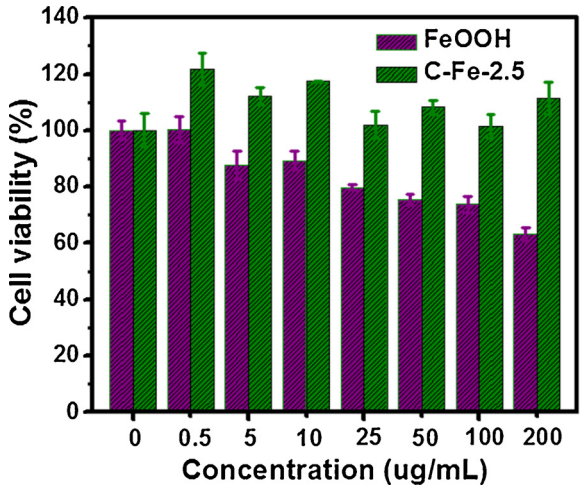

Fig. 7. Relative viability of A549 cells after incubation for 24 h with different concentrations of FeOOH and C-Fe-2.5.

4. Conclusions

In summary, CQDs/FeOOH composites exhibited enhanced NO removal efficiencies compared to pure FeOOH under both solar and visible light. Experimental and theoretical investigations showed that fast separation and transfer of photo-excited carriers due to the addition of CQDs were the dominant factors for effective light utilization and enhanced photoactivity. Good biocompatibility and low cytotoxicity of the composite was demonstrated. In addition, carbon- and iron-containing catalysts use highly abundant materials, unlike competing technologies such as Pt-cased catalysts. The findings of this study offer an effective design and fabrication strategy for developing photocatalytic materials for air purification.

Conflict of interest

Notes: The authors declare no competing financial interest.

Acknowledgements

This research was financially supported by the National Key Research and Development Program of China (grant No. 2016BBBMBYFA0203000), also partially supported by State Key Lab of Loess and Quaternary Geology (SKLLQGPY1605) and the National Science Foundation of China (Grant No. 41401567 and 41573138). Y.H. was supported by the "Hundred Talent Program" of the Chinese Academy of Sciences.

Appendix A. Supplementary data

Supplementary material related to this article can be found, in the online version, at doi:https://doi.org/10.1016/j.jhazmat.2018.04.071.

References

[1] P. Granger, V.I. Parvulescu, Catalytic NOx abatement systems for mobile sources: from three-way to lean burn after-Treatment technologies, Chem. Rev. 111 (2011) 3155–3207.
[2] R.J. Huang, Y.L. Zhang, C. Bozzetti, K.F. Ho, J.J. Cao, Y.M. Han, K.R. Daellenbach, J.G. Slowik, S.M. Platt, F. Canonaco, P. Zotter, R. Wolf, S.M. Pieber, E.A. Bruns, M. Crippa, G. Ciarelli, A. Piazzalunga, M. Schwikowski, G. Abbaszade, J. Schnelle-Kreis, R. Zimmermann, Z.S. An, S. Szidat, U. Baltensperger, I. El Haddad, A.S.H. Prevot, High secondary aerosol contribution to particulate pollution during haze events in China, Nature 514 (2014) 218–222.
[3] J. Lasek, Y.H. Yu, J.C.S. Wu, Removal of NOx by photocatalytic processes, J. Photochem. Photobiol. C 14 (2013) 29–52.
[4] W. Cui, J. Li, F. Dong, Y. Sun, G. Jiang, W. Cen, S.C. Lee, Z. Wu, Highly efficient performance and conversion pathway of photocatalytic NO oxidation on SrO-Clusters@Amorphous carbon nitride, Environ. Sci. Technol. 38 (2017) 10746–10753.
[5] S. Liu, Q. Hu, J. Qiu, F. Wang, W. Lin, F. Zhu, C.H. Wei, N. Zhou, G. Ouyang, Enhanced photocatalytic degradation of environmental pollutants under visible irradiation by a composite coating, Environ. Sci. Technol. 51 (2017) 5137–5145.
[6] H.B. Guo, A.S. Barnard, Naturally occurring iron oxide nanoparticles: morphology, surface chemistry and environmental stability, J. Mater. Chem. A 1 (2013) 27–42.
[7] J.L. Jambor, J.E. Dutrizac, Occurrence and constitution of natural and synthetic ferrihydrite, a widespread iron oxyhydroxide, Chem. Rev. 98 (1998) 2549–2585.
[8] Y. Zhang, S. Jiang, W. Song, P. Zhou, H. Ji, W. Ma, W. Hao, C. Chen, J. Zhao, Nonmetal P-doped hematite photoanode with enhanced electron mobility and high water oxidation activity, Energy Environ. Sci. 8 (2015) 1231–1236.
[9] X. Qiu, Z. Fang, B. Liang, F. Gu, Z. Xu, Degradation of decabromodiphenyl ether by nano zero-valent iron immobilized in mesoporous silica microspheres, J. Hazard. Mater. 193 (2011) 70–81.
[10] Y. Xu, M.A.A. Schoonen, The absolute energy positions of conduction and valence bands of selected semiconducting minerals, Am. Mineral 85 (2000) 543–556.
[11] L.V.C. Lima, M. Rodriguez, V.A.A. Freitas, T.E. Souza, A.E.H. Machado, A.O.T. Patrocínio, J.D. Fabris, L.C.A. Oliveira, M.C. Pereira, Synergism between n-type WO_3 and p-type δ-FeOOH semiconductors: high interfacial contacts and enhanced photocatalysis, Appl. Catal. B Environ. 165 (2015) 579–588.
[12] J. Liu, M. Zheng, X. Shi, H. Zeng, H. Xia, Amorphous FeOOH quantum dots assembled mesoporous film anchored on graphene nanosheets with superior electrochemical performance for supercapacitors, Adv. Funct. Mater. 26 (2016) 919–930.
[13] W. Xu, Z. Xie, Z. Wang, G. Dietrich, Y. Wang, Interwoven heterostructural Co_3O_4–carbon@FeOOH hollow polyhedrons with improved electrochemical performance, J. Mater. Chem. A 4 (2016) 19011–19018.
[14] J.X. Feng, H. Xu, Y.T. Dong, S.H. Ye, Y.X. Tong, G.R. Li, FeOOH/ Co/FeOOH hybrid nanotube arrays as high-performance electrocatalysts for the oxygen evolution reaction, Angew. Chem. 55 (2016) 3694–3698.
[15] J.X. Feng, S.H. Ye, H. Xu, Y.X. Tong, G.R. Li, Design and synthesis of FeOOH/CeO_2 heterolayered nanotube electrocatalysts for the oxygen evolution reaction, Adv. Mater. 28 (2016) 4698–4703.
[16] Z. Lian, W. Wang, G. Li, F. Tian, K. Schanze, H. Li, Pt-Enhanced mesoporous Ti^{3+}/TiO_2 with Rapid bulk to surface electron transfer for photocatalytic hydrogen evolution, ACS Appl. Mater. Interfaces 9 (2017) 16960–16967.
[17] Z. Lian, W. Wang, S. Xiao, X. Li, Y. Cui, D. Zhang, G. Li, H. Li, Plasmonic silver quantum dots coupled with hierarchical TiO_2 nanotube arrays photoelectrodes for efficient visible-light photoelectrocatalytic hydrogen evolution, Sci. Rep. 5 (2015) 10461.
[18] S. Wang, G. Li, M.K. Leung, Controlling charge transfer in quantum-size titania for photocatalytic applications, Appl. Catal. B: Environ. 215 (2017) 85–92.
[19] A.C. da Silva, M.R. Almeida, M. Rodriguez, A.R.T. Machado, L.C.A. de Oliveira, M.C. Pereira, Improved photocatalytic activity of δ-FeOOH by using H_2O_2 as an electron acceptor, J. Photochem. Photobiol. A: Chem. 332 (2017) 54–59.
[20] H. Qi, L. Cao, J. Li, J. Huang, Z. Xu, Y. Cheng, X. Kong, K. Yanagisawa, High pseudocapacitance in FeOOH/rGO composites with superior performance for High rate anode in Li-Ion Battery, ACS Appl. Mater. Interfaces 8 (2016) 35253–35263.
[21] L. Wang, N.T. Nguyen, Y. Zhang, Y. Bi, P. Schmuki, Enhanced solar Water splitting by swift charge separation in Au/FeOOH sandwiched single-crystalline Fe_2O_3 nanoflake photoelectrodes, ChemSusChem 10 (2017) 2720–2727.
[22] Y. Zhang, G. Jia, H. Wang, B. Ouyang, R.S. Rawat, H.J. Fan, Ultrathin CNTs@FeOOH nanoflake core/shell networks as efficient electrocatalysts for the oxygen evolution reaction, Mater. Chem. Front. 1 (2016) 709–715.
[23] C. Xue, H. Li, H. An, B. Yang, J. Wei, G. Yang, NiSx quantum dots accelerate electrons transfer in $Cd_{0.8}Zn_{0.2}S$ photocatalytic system via rGO nanosheet"bridge" towards visible-light-driven hydrogen evolution, ACS Catal. 8 (2018) 1532–1545.
[24] Y. Huang, Y. Liang, Y. Rao, D. Zhu, J.J. Cao, Z. Shen, W. Ho, S.C. Lee, Environment-Friendly carbon quantum Dots/$ZnFe_2O_4$ photocatalysts: characterization, biocompatibility, and mechanisms for NO removal, Environ. Sci. Technol. 51 (2017) 2924–2933.
[25] H. Ming, Z. Ma, Y. Liu, K. Pan, H. Yu, F. Wang, Z. Kang, Large scale electrochemical synthesis of high quality carbon nanodots and their photocatalytic property, Dalton Trans. 41 (2012) 9526–9531.
[26] L.W. Zhang, H.B. Fu, Y.F. Zhu, Efficient TiO_2 photocatalysts from surface hybridization of TiO_2 particles with graphite-like carbon, Adv. Funct. Mater. 18 (2010) 2180–2189.
[27] X. Han, Y. Han, H. Huang, H. Zhang, X. Zhang, R. Liu, Y. Liu, Z. Kang, Synthesis of carbon quantum dots/SiO_2 porous nanocomposites and their catalytic ability for photo-enhanced hydrocarbon selective oxidation, Dalton Trans. 42 (2013) 10380–10383.
[28] H. Li, R. Liu, Y. Liu, H. Huang, H. Yu, H. Ming, S. Lian, S.T. Lee, Z. Kang, Carbon quantum dots/Cu_2O composites with protruding nanostructures and their highly efficient (near) infrared photocatalytic behavior, J. Mater. Chem. 22 (2012) 17470–17475.
[29] H. Yu, H. Zhang, H. Huang, Y. Liu, H. Li, H. Ming, Z. Kang, ZnO/carbon quantum dots nanocomposites: one-step fabrication and superior photocatalytic ability for toxic gas degradation under visible light at room temperature, N. J. Chem. 36 (2012) 1031–1035.
[30] H. Zhang, H. Ming, S. Lian, H. Huang, H. Li, L. Zhang, Y. Liu, Z. Kang, S.T. Lee, Fe_2O_3/carbon quantum dots complex photocatalysts and their enhanced photocatalytic activity under visible light, Dalton Trans. 40 (2011) 10822–10825.
[31] J. Liu, H. Zhang, D. Tang, X. Zhang, L. Yan, Y. Han, H. Huang, Y. Liu, Z. Kang, Carbon quantum dot/silver nanoparticle/polyoxometalate composites as

photocatalysts for overall water splitting in visible light, Chemcatchem 6 (2015) 2634–2641.
[32] R. Liu, H. Huang, H. Li, Y. Liu, J. Zhong, Y. Li, S. Zhang, Z. Kang, Metal Nanoparticle/Carbon quantum dot composite as a photocatalyst for high-efficiency cyclohexane oxidation, ACS Catal. 4 (2014) 328–336.
[33] H. Zhang, H. Huang, H. Ming, H. Li, L. Zhang, Y. Liu, Z. Kang, Carbon quantum dots/Ag_3PO_4 complex photocatalysts with enhanced photocatalytic activity and stability under visible light, J. Mater. Chem. 22 (2012) 10501–10506.
[34] S.Y. Lim, W. Shen, Z.Q. Gao, Carbon quantum dots and their applications, Chem. Soc. Rev. 44 (2015) 362–381.
[35] Z. Zhang, T. Zheng, X. Li, J. Xu, H. Zeng, Progress of carbon quantum dots in photocatalysis applications, Part. Part. Syst. Charact. 33 (2016) 457–472.
[36] X. Qian, M. Ren, Y. Zhu, D. Yue, Y. Han, J. Jia, Y. Zhao, Visible light assisted heterogeneous fenton-like degradation of organic pollutant via α-FeOOH/ Mesoporous carbon composites, Environ. Sci. Technol. 51 (2017) 3993–4000.
[37] H.Y. Wu, C.C. Mi, H.Q. Huang, B.F. Han, J. Li, S.K. Xu, Solvothermal synthesis of green-fluorescent carbon nanoparticles and their application, J. Lumin. 132 (2012) 1603–1607.
[38] M. Segall, P.J.D. Lindan, M.J. Probert, C.J. Pickard, P.J. Hasnip, S.J. Clark, MCPayne, first-principles simulation: ideas, illustrations and the CASTEP code, J. Phys.: Condens. Matter 14 (2002) 2717–2744.
[39] J.P. Perdew, K. Burke, M. Ernzerhof, Generalized gradient approximation made simple, Phys. Rev. Lett. 77 (1996) 3865–3868.
[40] F. Zhang, X. Feng, Y. Zhang, L. Yan, Y. Yang, X. Liu, Photoluminescent carbon quantum dots as a directly film-forming phosphor towards white LEDs, Nanoscale 8 (2016) 8618–8632.
[41] J. Di, J. Xia, M. Ji, H. Li, H. Xu, H. Li, R. Chen, The synergistic role of carbon quantum dots for the improved photocatalytic performance of Bi_2MoO_6, Nanoscale 7 (2015) 11433–11443.
[42] J.Q. Pan, Y.Z. Sheng, J.X. Zhang, J.M. Wei, P. Huang, X. Zhang, B.X. Feng, Preparation of carbon quantum dots/TiO_2 nanotubes composites and their visible light catalytic applications, J. Mater. Chem. A 2 (2014) 18082–18086.
[43] T.C. Araújo, Hd.S. Oliveira, J.J.S. Teles, J.D. Fabris, L.C.A. Oliveira, J.P. de Mesquita, Hybrid heterostructures based on hematite and highly hydrophilic carbon dots with photocatalytic activity, Appl. Catal. B: Environ. 182 (2016) 204–212.
[44] H. AbdelSamad, P.R. Watson, An XPS study of the adsorption of chromate on goethite (alpha-FeOOH), Appl. Surf. Sci. 108 (1997) 371–377.
[45] H. Abdel-Samad, P.R. Watson, An XPS study of the adsorption of lead on goethite (alpha-FeOOH), Appl. Surf. Sci. 136 (1998) 46–54.
[46] J.K. Leland, A.J. Bard, Photochemlstry of colloidal semiconducting iron oxlde polymorphs, J. Phys. Chem. 91 (1987) 5083–5087.
[47] K. Fujiwara, U. Müller, S.E. Pratsinis, Pd subnano-clusters on TiO_2 for solar-light removal of NO, ACS Catal. 6 (2016) 1887–1893.
[48] Q. Zhang, Y. Huang, S. Peng, Y. Zhang, Z. Shen, J.-j. Cao, W. Ho, S.C. Lee, D.Y.H. Pui, Perovskite $LaFeO_3$ -$SrTiO_3$ composite for synergistically enhanced NO removal under visible light excitation, Appl. Catal. B: Environ. 204 (2017) 346–357.
[49] R. Long, D. Casanova, W.H. Fang, O.V. Prezhdo, Donor – Acceptor interaction determines the mechanism of photoinduced electron injection from graphene quantum dots into TiO_2: π-stacking supersedes covalent bonding, J. Am. Chem. Soc. 139 (2017) 2619–2629.
[50] Q. Tian, J. Zhuang, J. Wang, L. Xie, P. Liu, Novel photocatalyst, $Bi_2Sn_2O_7$, for photooxidation of As (III) under visible-light irradiation, Appl. Catal. A: Gen. 425–426 (2012) 74–78.
[51] L. Yu, G. Zhang, C. Liu, H. Lan, H. Liu, J. Qu, Interface stabilization of under-coordinated iron centers on manganese oxides for nature-inspired peroxide activation, ACS Catal. 8 (2018) 1090–1096.
[52] Y. Gao, Y. Huang, Y. Li, Q. Zhang, J.-j. Cao, W. Ho, S.C. Lee, Plasmonic Bi/$ZnWO_4$ microspheres with improved photocatalytic activity on NO removal under visible light, ACS Sustain. Chem. Eng. 4 (2016) 6912–6920.